journal of the mechanical behavior of biomedical materials 125 (2022) 104905

Contents lists available at ScienceDirect

Journal of the Mechanical Behavior of Biomedical Materials

journal homepage: www.elsevier.com/locate/jmbbm

Research Paper

Creep behavior of human knee joint determined with high-speed biplanar video-radiography and finite element simulation

S. Uzuner [a,*], G. Kuntze [b], L.P. Li [c,**], J.L. Ronsky [c], S. Kucuk [d]

[a] Department of Mechatronics, Dr. Engin PAK Cumayeri Vocational School, University of Duzce, Cumayeri, Duzce, Marmara, 81700, Turkey
[b] Faculty of Kinesiology, University of Calgary, 2500 University Drive, N.W, Calgary, Alberta, Canada, T2N 1N4
[c] Department of Mechanical and Manufacturing Engineering, University of Calgary, 2500 University Drive, N.W, Calgary, Alberta, Canada, T2N 1N4
[d] Department of Biomedical Engineering, University of Kocaeli, Izmit, Kocaeli, Marmara, 41001, Turkey

ARTICLE INFO

Keywords:
Articular cartilage
Biplanar videoradiography
Fibril-reinforced model
Fluid pressure
In-vivo cartilage creep
Tibiofemoral joint

ABSTRACT

Creep and relaxation of knee cartilage and meniscus have been extensively studied at the tissue level with constitutive laws well established. At the joint level, however, both experimental and model studies have been focused on either elastic or kinematic responses of the knee, where the time-dependent response is typically neglected for simplicity. The objectives of this study were to quantify the in-vivo creep behavior of human knee joints produced by the cartilaginous tissues and to use the relevant data to validate a previously proposed poromechanical model.

Two participants with no history of leg injury volunteered for 3T magnetic resonance imaging (MRI) of their unloaded right knees and for biplanar video-radiography (BVR) of the same knees during standing on an instrumented treadmill for 10 min. Approximately 550 temporal data points were obtained for the in-vivo displacement of the right femur relative to the tibia of the knee. Models of the bones and soft tissues were derived from the MRI. The bone models were used to reconstruct the 3D bone kinematics measured using BVR. Ground reaction forces were simultaneously recorded for the right leg, which were used as input for the subject-specific finite element knee models. Cartilaginous tissues were modeled as fluid-saturated fibril-reinforced materials.

In-vivo creep of the knee was experimentally observed for both participants, i.e., the joint displacement increased with time while the reaction forces at the foot were approximately constant. The creep displacements obtained from the finite element models compared well with the experimental data when the tissue properties were calibrated (Pearson correlation coefficient = 0.99).

The results showed the capacity of the poromechanical knee model to capture the creep response of the joint. The combined experimental and model study may be used to understand the fluid-pressure load support and contact mechanics of the joint using material properties calibrated from the displacement data, which enhance the fidelity of model results.

1. Introduction

Knee osteoarthritis (OA) is a degenerative pathology of the articular cartilages of the femur, tibia and patella, and is associated with pain (Barron and Rubin, 2007), disability (Felson et al., 1987), and reduced quality of life (Salaffi et al., 2005). The disease pathway is influenced by numerous factors including age, obesity, and joint trauma (Felson, 2006; Lohmander et al., 2007). Prospective studies indicate a 10-fold increase in the risk of developing knee OA within 12–20 years post knee injury (Lohmander et al., 2007). Mechanical and biological changes are theorized to alter the structure and composition of cartilage after injury, causing cartilage swelling and softening, which are recognized early signs of cartilage degeneration (Roos et al., 1998; Zhang et al., 2003; Waite et al., 2005). Such softening and swelling of cartilage may reduce the load-bearing capacity of cartilage and increase the susceptibility of cartilage to mechanical damage (Maniwa et al., 2001; Buck et al., 2010; Eckstein and Wirth, 2011). It is thus essential to understand load bearing in the knee joint.

The load-bearing capacity of cartilage and meniscus is regulated by

* Corresponding author.
** Corresponding author.
E-mail addresses: sabriuzuner@duzce.edu.tr (S. Uzuner), leping.li@ucalgary.ca (L.P. Li).

https://doi.org/10.1016/j.jmbbm.2021.104905
Received 4 May 2021; Received in revised form 22 September 2021; Accepted 12 October 2021
Available online 16 October 2021

Nomenclature

BVR	Biplanar video-radiography (or dual fluoroscopy)
FE/FEM	Finite element/Finite element method
MRI	Magnetic resonance imaging
OA	Osteoarthritis
TF	Tibiofemoral (joint)
2D/3D	Two/Three dimensional

the solid-fluid interaction depending on joint loading rates (Rodriguez and Li, 2017). However, most joint models have ignored the fluid phase in the cartilaginous tissues assuming that the knee joint is under instantaneous load and thus only focused on the elastic response of the joint (Bei et al., 2004; Kiapour et al., 2014; Shriram et al., 2017; Trad et al., 2017). Using in-vitro and in-situ tests of tissue or whole joint specimens, it has been observed that cartilage exhibits creep and relaxation behavior as a result of the interstitial fluid flow in the solid matrix (Cao et al., 2006; Boettcher et al., 2016; Rodriguez and Li, 2017; Stolberg-Stolberg et al., 2018). Finite element (FE) knee joint models that consider fluid-induced creep behavior of cartilage and meniscus have been reported recently (Gu and Li, 2011; Dabiri and Li, 2013). Both creep and relaxation behavior of the intact and meniscectomized tibiofemoral (TF) joints were examined (Kazemi et al., 2011; Kazemi and Li, 2014). These behaviors were observed to be primarily associated with fluid flow and pressurization and have been referred to as poromechanical (Uzuner et al., 2020).

Finite element methods are a valuable approach to assess the consequences of external loading of the human knee joint on factors such as strain and stress, as well as contact and fluid pressures that cannot be measured directly in human participants. On the other hand, experimental studies of the knee joint have an important role in both providing input data for and validating FE models. Most FE studies performed at the knee joint level have either not been validated or only been indirectly validated with data from independent studies performed under similar force and boundary conditions. Such indirect validations compare the predicted FE results with data from studies in which the loading conditions may be similar but are based on different joint specimens or research participants (Cooper et al., 2019). This approach raises concerns over the reliability of model findings (Erdemir et al., 2019), as factors including joint geometry, age, and sex may influence the knee joint mechanics (Eckstein et al., 2009). Using the same knees for model constructions and validation experiments may reduce these concerns.

Most mechanical tests of articular cartilage reported over the past four decades were performed using tissue specimens in vitro. For example, a commercial shear rheometer was used to determine the creep behavior of cartilage specimens extracted from the patellofemoral groove of male ovine stifle joints (Boettcher et al., 2014). Creep recovery of cartilage plugs was also characterized for femoral condyles of male bovine knees after a creep load of 110 kPa was applied for 120min (Stolberg-Stolberg et al., 2018). Creep indentation testing has also been commonly reported in animal joints where cartilage integrity is conserved (e.g., Cao et al., 2006). However, the contact and loading conditions in these studies are not physiological.

Utilizing the intact knee joint enables the contribution of multiple contacts between complex tissues that work together for load sharing to be captured (Uzuner et al., 2020). In-situ creep tests of porcine knee joints were used to understand the time-dependent behavior of the joint produced by the cartilaginous tissues (Rodriguez and Li, 2017). Moreover, in-situ cartilage deformation and thickness were measured using cadaver and animal knee joints under creep load conditions (Herberhold et al., 1998, 1999; Song et al., 2006; Shiomi et al., 2012). In-vivo studies are more representative of physiological conditions than in-situ studies, owing to native boundary conditions and the integrity of the knee joint (Hosseini et al., 2010). In-vivo time-dependent contact deformation of knee cartilage during a prolonged standing was first estimated using a biplanar video-radiography (BVR) and magnetic resonance imaging (MRI) technique, where full bodyweight was quickly applied and maintained for 300s (Hosseini et al., 2010). Similarly, in-vivo contact deformation of tibiofemoral (TF) articular cartilage during the stance phase of gait was examined using a combined BVR and statistical shape modeling technique (Liu et al., 2010; Li et al., 2014). In-vivo healthy and early OA TF cartilage deformation was also obtained using BVR (Sharma et al., 2015). MRI compatible loading devices have been used to evaluate articular cartilage deformation non-invasively under axial load (Schoenbauer et al., 2015; Wang et al., 2015; Chan et al., 2016). Further, a C-arm-based cone-beam CT system was used to measure the in-vivo time-dependent creep of tibial cartilage during static weight-bearing (Choi et al., 2016).

These in-vivo experimental studies provide valuable information such as altered cartilage thicknesses and average tissue deformation in the knee joint under physiological loading. However, they have not been used to validate FE models or combined with FE models to predict mechanical behavior that are not available from experiments. FE methods allow determination of the spatial distribution of stress, strain, and fluid pressure, which are currently challenging to measure experimentally (Halonen et al., 2014). Few studies have detailed creep behavior of cartilages at the joint level or validated FE models with in-vivo experimental results obtained from the same joints. FE modeling was used to provide insight into the creep strains in the tibial cartilage using TF joint compression obtained at 0, 1, 5, and 30 min of standing (Halonen et al., 2014). Additionally, the effect of spatial variation of fixed charge density on the mechanical response of the tibial cartilage in vivo was investigated using a 7T sodium MRI and FE model for 13-min static loading of half bodyweight (Räsänen et al., 2016). Consequently, in-vivo measurements have enhanced the fidelity of FE results and FE models have expanded the research findings beyond in-vivo experimentation. Inspired by these studies and recent progress in in-vivo measurement, the objectives of the present study were to provide a perspective on the time-dependent creep behavior of the knee joint during a prolonged standing and to validate a poromechanical finite element model of the knee joint. Our FE models were constructed for the same knees of the participants recruited for the MRI and BVR measurements. Furthermore, an essentially continuous creep displacement of the joint was obtained as a function of time to enhance the fidelity in our model validation.

2. Methods

Fibril-reinforced poromechanical FE models of the right TF joints of two healthy participants were developed to simulate the creep behavior of human knee obtained from 10-min joint loading during standing with intermittent BVR. The ground reaction forces measured in vivo from a force plate were used as the input to these models. The vertical displacements of the proximal femur relative to the distal tibia determined by the models were then compared with those obtained from the BVR measurements. Following model validation, the mechanics of the knee joint, including fluid and contact pressures, were theoretically examined under the standard creep load (i.e., ramp and then constant load) up to the equilibrium state. The workflow chart (Fig. 1) shows an overview of the BVR measurement protocol and the FE method.

2.1. Human measurements with biplanar video-radiography

Two healthy study participants with no history of leg injury volunteered for this study (Participant A: 24-year-old female, weight 59 kg; Participant B: 25-year-old male, weight 68 kg), which was approved by the local ethics board (REB15-1165). The BVR system consists of two high-speed high-resolution video cameras, two signal generators, two x-

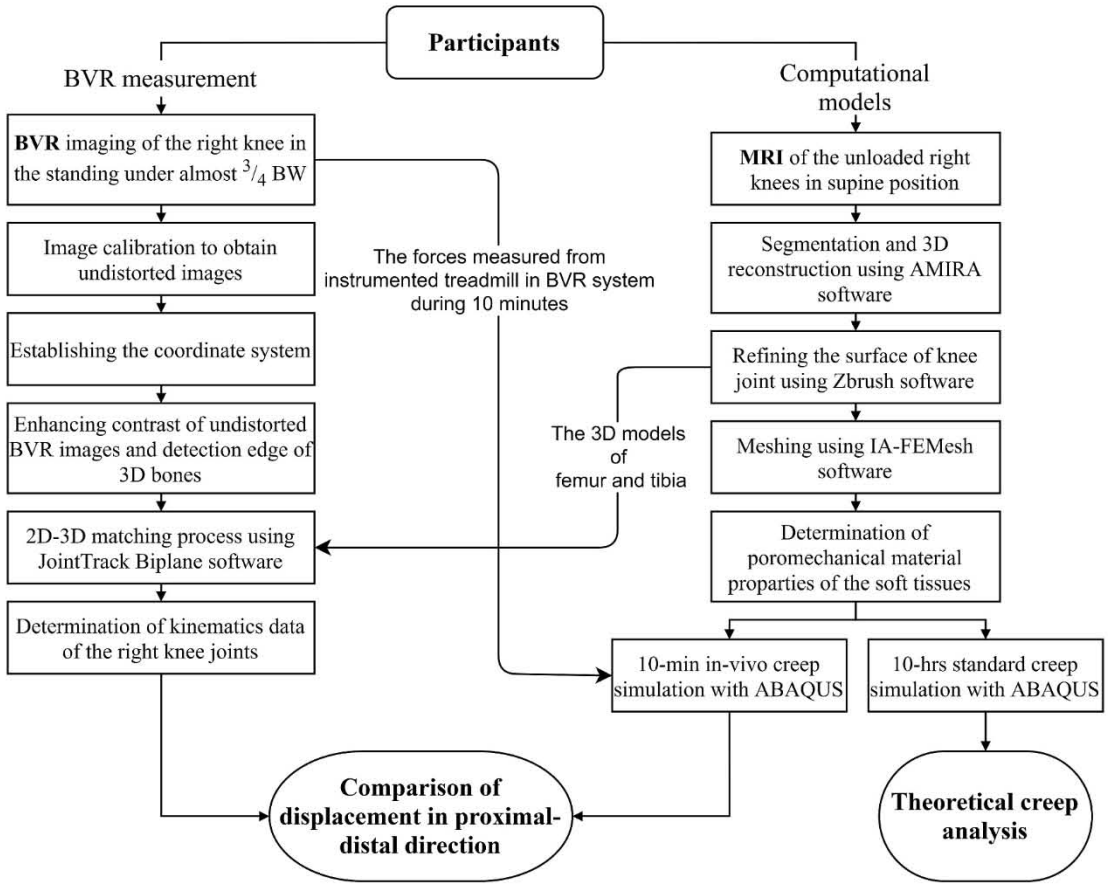

Fig. 1. Workflow chart of the combined experimental and computational study. Custom programs developed using MATLAB software were used to calibrate images, establish coordinate systems, enhance image contrast and detect edges of tissues. The biplanar video-radiography (BVR) measurement was performed for 10 min only, but additional finite element analyses were done for 10 h.

ray sources, two image intensifiers and an instrumented treadmill (Fig. 2a). In-vivo testing for each research participant was conducted on two separate days. On the set up and rehearsal day, after completing the informed consent form, participants attended the BVR lab for a measurement task familiarization session without X-rays. Approximate creep loading for the right knee was produced with their partial bodyweight as follows. Participants were initially asked to stand on their left foot on a box placed on the top of the instrumented treadmill (Bertec, USA) without applying force to their right leg. Participants were able to use the treadmill handrails for minimal support and balance. When instructed, the participants then lowered their fully extended right leg to contact the treadmill surface. Participants were instructed to slowly and smoothly increase the force applied to the right leg so that they were predominantly weight bearing on the right leg, with the transition from left leg to right leg weight bearing lasting about 10 s. This slow load application eliminates the difficulty in modeling convergence caused by large stress/strain increments and fluid pressure gradients in the tissues associated with a rapidly applied force to the knee. No external control on the loading speed and magnitude of loading on the right leg was provided. Participants maintained this weight bearing posture for 10 min.

In-vivo data collections were conducted on the second day in the early morning to minimize the effect of cartilage loading history prior to testing. Participants were asked to minimize load bearing on the day prior to testing (no sports) as well as in the morning on the day of testing (necessary indoor walking only prior to transportation to the testing facility). Participants were brought to the MRI center by car and wheelchair. They remained seated for 30 min prior to a 3T MRI to minimize load bearing in the right legs. Participants were then assisted onto the MRI scanner (Discovery MR750, GE, USA) table and lay in a supine position. A high-resolution MRI sequence was used to image the right knee (3D FIESTA: fast imaging employing steady-state acquisition; knee coil was used; Slice thickness: 1 mm; 200 slices; Slice spacing: 0.5 mm; Field of view: 24 × 24 cm^2; Matrix: 512 × 512 pixels).

Following MRI scans, participants were transferred to the BVR lab using a wheelchair, avoiding right leg external loading. Participants were then fit with a custom knee brace to limit right knee flexion. The BVR measurement protocol consisted of continuous imaging at 6 Hz (the lowest system frequency) for the first 60 s, followed by 2-s short imaging bursts at 6Hz every 30 s. A total of 550 image pairs were collected for each participant. This image acquisition procedure was selected to capture the high tissue deformation in the first minute of loading (Hosseini et al., 2010; Uzuner et al., 2019) and to minimize the X-ray exposure to the participants over the 10-min measurement. The X-ray exposure for each participant was estimated to be lower than 0.5 mSv.

2.2. Data processing on biplanar video-radiography

Six-degree-of-freedom (6-DOF) bone kinematics were reconstructed from BVR images using a 2D-3D registration approach. 3D bone and soft tissue models for the TF joint were generated from MRI using manual image segmentation in AMIRA software (Thermo Fisher Scientific, USA). The models were then refined using ZBrush software (Pixologic, USA) to minimize errors introduced in surface reconstruction. Local coordinate systems for the femur and tibia were determined using anatomical features (Grood and Suntay, 1983). BVR image sequences were distortion corrected, calibrated, and processed (Lichti et al., 2015). In this procedure, all X-ray images were corrected for lens distortion

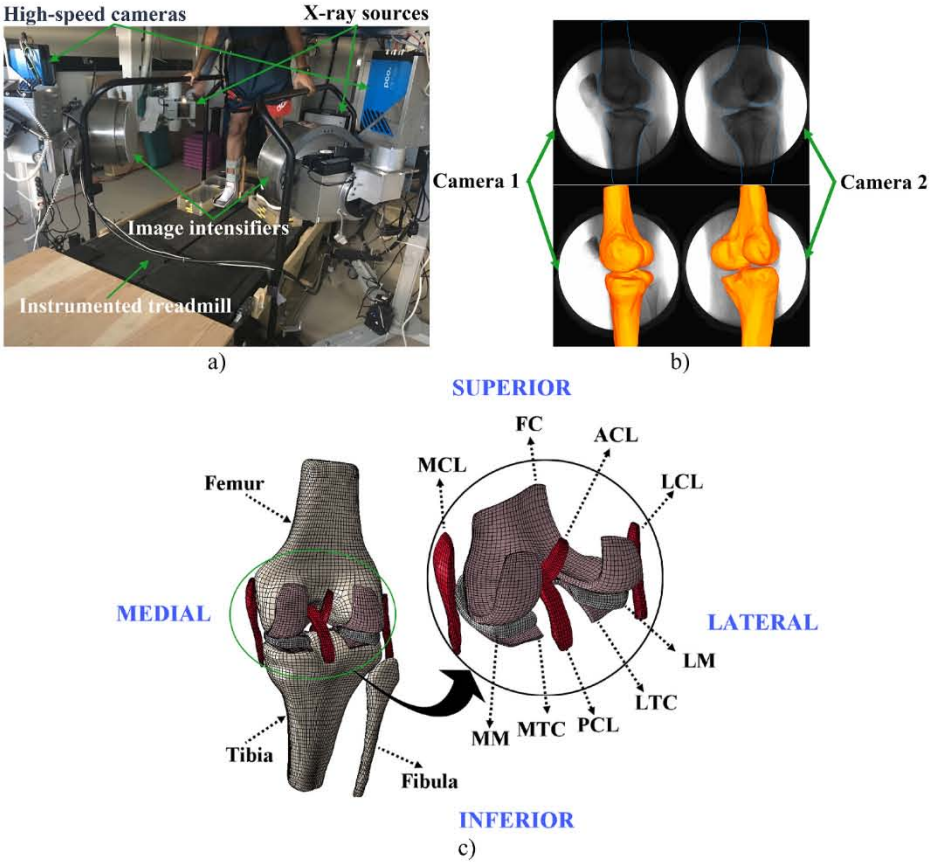

Fig. 2. Schematic of the measurement and modeling. a) High-speed BVR imaging system; b) Matching the 3D models with embedded coordinate system to the corresponding corrected BVR images (Participant B); and c) The FE models of the right TF joint with meshes for Participant B. The element numbers of the bones, articular cartilages, menisci, and ligaments were, respectively, 12,786, 13,412, 6175, and 4105 for the model of Participant B. The element numbers for Participant A were similar. Abbreviations used in the legend: MCL and LCL, medial and lateral collateral ligaments; ACL and PCL, anterior and posterior cruciate ligaments; FC, femoral cartilage; MTC and LTC, medial and lateral tibial cartilages; MM and LM, medial and lateral meniscus.

using images obtained from a perforated steel grid and *Undistorter* software (Brown University, USA). Thereafter, a direct linear transform approach (Allard et al., 1995; Chen et al., 1994; Shapiro, 1978) was used to calibrate X-ray source and X-ray image pairs using a custom built calibration object with custom software implemented in MATLAB (MathWorks, USA). A MATLAB algorithm was newly developed to enhance the contrast of BVR images to show clearly the bone edges and reduce error in the 2D-3D manual matching process. The 6-DOF kinematics of the femur and tibia were obtained from the two X-ray images using manual 2D-3D registration in Joint Track Biplane software (University of Florida, USA). Here, the bone models of the femur and tibia were placed in a virtual environment and the model positions were adjusted so that the bone model contours match those of the underlying X-ray images (Fig. 2b). The resultant poses were saved to provide the 3D transformation matrices (i.e. translations and rotations) for each bone at each capture image frame.

2.3. Subject-specific finite element models

FE meshes of the two TF joint models were generated with IA-FEMesh (University of Iowa, USA) using the MRI reconstructed geometries. The subject-specific knee joint models contain the bony structures (femur, tibia, and fibula) and the soft tissues (femoral and tibial cartilages, menisci, four main ligaments) (Fig. 2c). The cartilages and ligaments were discretized in 4 layers and the menisci in 5 layers of elements in the thickness directions. This mesh was selected to obtain convergent results according to a previously performed mesh sensitivity analysis (Uzuner et al., 2020). The knee joint model consisted of 32,579 elements for Participant A and 36,478 elements for Participant B. ABAQUS software (ABAQUS 6.17, Simulia, France) was used for the finite element analysis. The element types were selected as quadrilateral (R3D4), hexahedral porous (C3D8P), and continuum solid (C3D8) elements for the bones, cartilaginous tissues, and ligaments, respectively. The use of pure hexahedral elements for cartilaginous tissues facilitates faster convergence in the contact analysis as compared to tetrahedral elements, when fluid pressurization for the tissues is considered (Dassault Systems and Abaqus, 2016).

2.4. Material properties

The bony structures were considered as rigid bodies since they are much stiffer compared to soft tissues. Articular cartilages and menisci of the knee joints were modeled as poromechanical to consider creep behaviors induced by fluid pressurization. The constitutive equations for the poromechanical model were defined previously (Kazemi and Li, 2014). The cartilaginous tissues were defined as nonlinear fibril-reinforced materials and modeled as fluid-saturated porous elements owing to the time-dependent creep observed in knee joints (Rodriguez and Li, 2017). The non-fibrillar parts of the solid matrices in the soft tissues were assumed isotropic and hyperelastic. Ligaments were modeled as fibril-reinforced solids, as the fluid pressurization in tensile elements is negligible. The collagen fibrillar matrix is of great tensile stiffness, which plays an important role in fluid pressurization during tissue compression. Thus, the nonlinear properties of the fibrillar matrix were taken into account for the cartilaginous tissues and ligaments in the FE knee models (Gu and Li, 2011). The collagen matrix was modeled as a quasi-linear viscoelastic and orthotropic fibrillar matrix. Additionally, the fiber orientation in the femoral cartilage and menisci was chosen on a site specific basis using data reported in literature (Below et al., 2002). The fiber directions in the tibial cartilages were assumed to align in the local x-axis directions as no specific orientation data was found from the literature. The variation in fiber orientation with tissue depth was ignored. The soft tissue permeability was defined as orthotropic.

The material properties of soft tissues for both knee models (Table 1)

Table 1
Material properties of the fibrillar and nonfibrillar matrices of soft tissues in both knee models. The fibril direction was aligned in the x-axis of the local coordinate system, in which higher permeability was assumed (Buck et al., 2010). The nonlinear property of the tissue is modeled with B in this table. The reduced relaxation function, $G(t)$, determines the rate of creep or relaxation of the collagen fibrillar matrix. For simplicity, a discrete spectrum of the function is used here by introducing small, medium, and large time constants, λ^i (Li and Herzog, 2004). Moreover, the strain-rate dependency is accounted for by the interplay between fluid pressurization and nonlinear fibril reinforcement (Li et al., 2002).

		Collagen fibrillar matrix $\sigma = A\varepsilon + B\varepsilon^2$				Non-fibrillar matrix (isotropic)	
		Primary fiber direction (x) [MPa]		Perpendicular directions (y,z) [MPa]		Young's modulus [MPa]	Poisson's ratio
		A	B	A	B		
Participant A	Femoral Cartilage	4	1500	2	750	0.60	0.36
	Tibial Cartilage	4	1500	4	1500	0.60	0.36
	Menisci	28	1500	5	750	0.50	0.36
	Ligaments	46	1118	0	0	2	0.30
Participant B	Femoral Cartilage	2	1000	0.9	480	0.26	0.36
	Tibial Cartilage	2	1000	2	1000	0.26	0.36
	Menisci	12	1500	2	750	0.50	0.36
	Ligaments	46	1118	0	0	2	0.30
Weight constants (g^m)		g^1=0.3; g^2=1.7; g^3=0.5					
Characteristic times (λ^m)		λ^1=10; λ^2=100; λ^3=1000			$G(t) = 1 + \sum_m g^m \exp(\frac{-t}{\lambda^m})$		
Permeability [mm^4/Ns]		Darcy's law: $\phi^f v_x = -k_x p_x$; k_x=0.0002; k_y= k_z =0.0001. ϕ^f is porosity.					

were obtained by calibration based on values obtained from the literature (Woo et al., 1976; Tissakht and Ahmed, 1995; Li et al., 2002, 2003; Peña et al., 2006; Shirazi et al., 2008) to match the bone kinematics obtained from BVR measurements. The calibration approach involved tuning input parameters by comparing the FE model results with the experimental data (Cooper et al., 2019). Consequently, different material properties were selected for the two FE models.

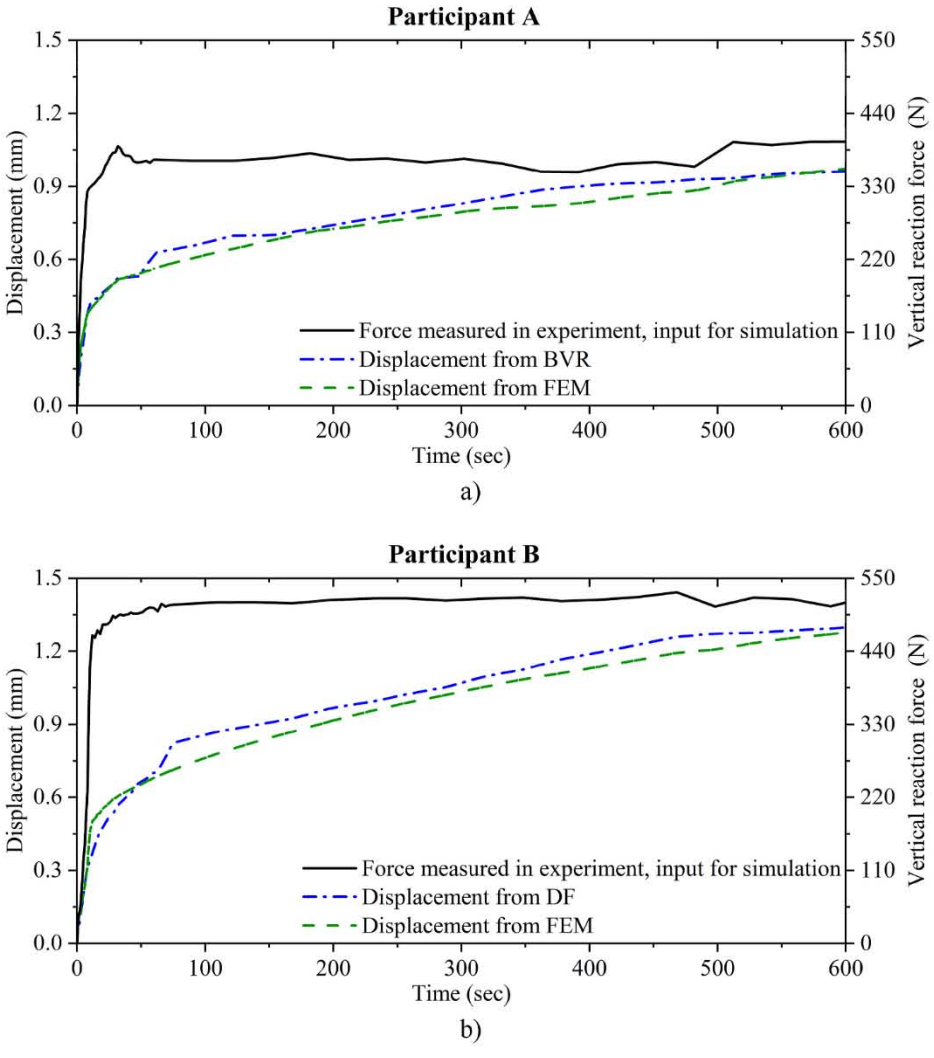

Fig. 3. Comparison of BVR measurement with finite element simulation for **a)** Participant A; and **b)** Participants B. The vertical ground reaction forces were measured by the force plate instrumented in the treadmill, and used as input for the finite element simulation. The vertical displacement of femur during the BVR test was calculated with respect to the tibia, because only the relative displacement affects the knee joint compression. Similarly, the tibia was fixed in all directions in the FE analyses to simulate the BVR test.

2.5. Load and boundary conditions

Two types of FE analyses were performed in the present study, in which the load and boundary conditions were similar to that in the BVR measurements. The first analysis was used to simulate the BVR measurement results (i.e., joint displacements) and determine the corresponding tissue properties. In this approach the ground reaction forces measured during the BVR test as functions of time (Fig. 3) were used as input for the FE simulation. The tissue properties were adjusted to match the BVR measured joint displacement. In the second analysis, a standard creep loading protocol was used to better demonstrate the full range of the nonlinear time-dependent behavior of the joint. Similar to the measurement, the standard creep loading consisted of a zero start ramp load of 12s (32.5N/s of loading rate) followed by a constant load for 10 h (Fig. 4). The constant load was chosen to be 390N, which was the maximum vertical force measured during the BVR measurement of Participant A. This load was applied for the models of both participants in the second type of analyses for convenience of comparison. The compressive loads were applied on the femur in the proximal-distal direction. The femur was fixed in other translation and rotation directions. The tibia and fibula were fully constrained in all directions. The TIE contact option in ABAQUS (i.e., no relative motion between contact surfaces) was used to fix the femoral cartilage to the femur, the tibial cartilage to the tibia, the meniscal horn to the tibial plateau and the ligaments to the adjacent bones to simulate the real attachment in human knee joint. Six contact pairs were defined, three on the medial and three on the lateral compartments of knee joint: femoral cartilage-menisci, femoral-tibial cartilages, and menisci-tibial cartilage (Fig. 2c). The soil consolidation procedure in ABAQUS was used to simulate the interaction between the solid and fluid.

3. Results

The maximum vertical ground reaction force measured during participant standing was 390N (Figs. 3a) and 520N (Fig. 3b) for Participants A and B respectively. During standing experiments, the vertical reaction force reached its plateau at about 8 and 12 s for Participants A and B respectively. The vertical reaction force then remained almost constant during the remaining 10-min testing duration (Fig. 3), thereby representing an approximate in-vivo creep testing protocol. The corresponding loading rate was 48.8 N/s and 43.3 N/s for Participants A and B, respectively. The experimental displacement of the femur relative to the tibia was successfully modeled with the FEM. At 10 min, vertical displacement was 0.96 mm and 1.30 mm for Participants A and B respectively.

The creep displacements were also obtained with FE knee models under a standard creep loading of 390N to extend the results beyond 10 min (Fig. 4). The maximum displacements predicted with the FEM were

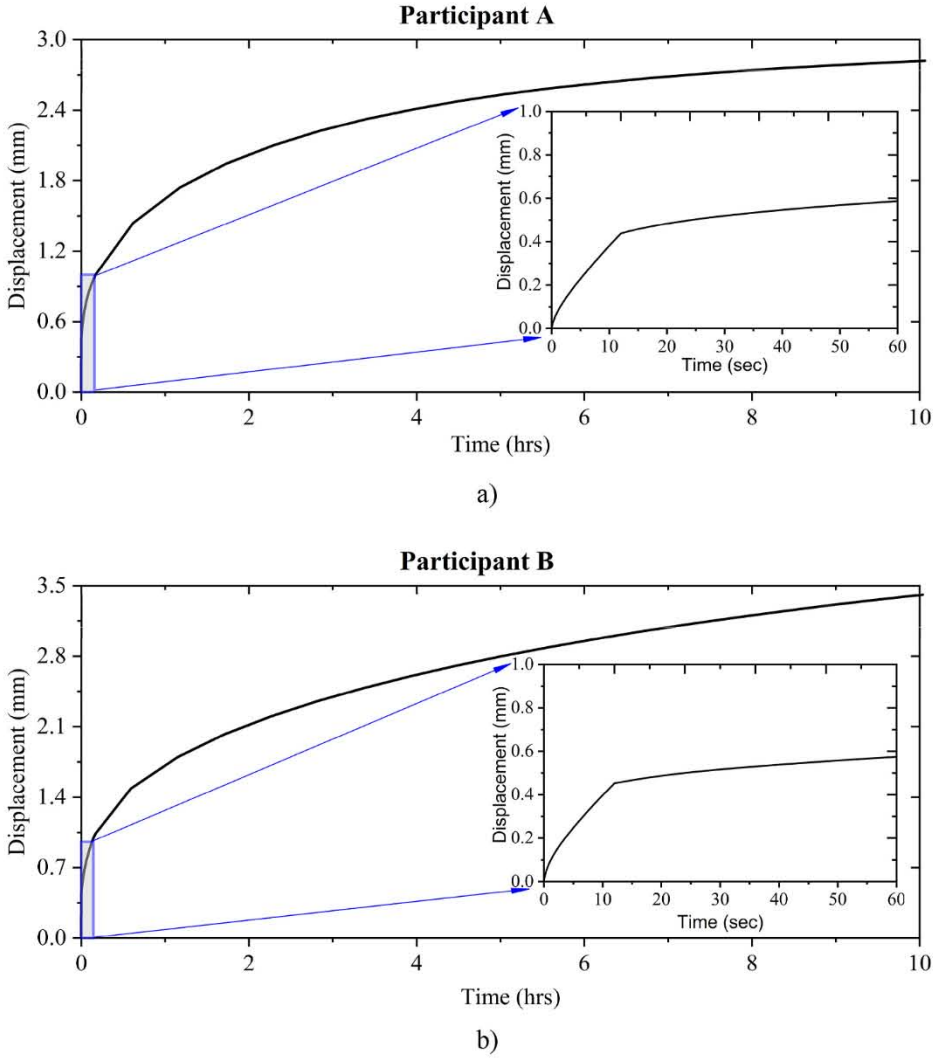

Fig. 4. Vertical displacement of the knee joint developed during a standard creep loading of 390N applied in 12s as determined from the FE models of: a) Participant A; and b) Participant B.

2.82 and 3.41 mm at the long term (10hrs) for Participant A and B respectively (Fig. 4). The maximum strains in the surface of tibial cartilages at 12s were 13% and 14% for Participants A and B respectively. These maximum strains occurred in the medial compartment for Participant A and in the lateral compartment for Participant B. The strains increased with creep and were 40% and 43% at 10hrs for Participants A and B respectively (Fig. 5).

As creep developed, the maximum contact pressures decreased substantially in each tibial cartilage for both participants, with the pressure in the lateral cartilage higher than that in the medial cartilage (Fig. 6). For example in the knee of Participant A, the peak pressure of 1.80 MPa at 12s decreased to 0.85 MPa at 10hrs in the lateral tibial cartilage. The pressures were higher in the knee of Participant A relative to that of Participant B when the same 390N force was applied: 52% and 42% higher respectively, in the lateral and medial compartments at 12s (Fig. 6). The contact areas increased, whereas the average contact pressures decreased with creep for both participants. For example, for the lateral knee compartment of Participant A, the contact area increased by 62% during creep, while the contact pressure decreased by 38% (Table 2). Substantial joint congruence was achieved in 2s indicated by a slow increase in the contact area after 2s of loading, e.g., for Participant A, the total contact area was 550 mm^2 at 2s, compared to 770 mm^2 at 600s and 970 mm^2 at 10hrs. While the location of higher contact pressure did not change with time between the tibial compartments for Participant B, it shifted from the lateral to medial compartments for Participant A (Fig. 7).

At 12s, the maximum fluid pressures in the lateral tibial cartilage compartments were 1.84 and 1.30 MPa for Participants A and B, respectively (Fig. 8). Lower maximum fluid pressures of 1.33 and 0.97 MPa were observed in the medial tibial compartment at 12s, for the Participants A and B, respectively. Consistent with the contact pressures, the maximum fluid pressures decreased dramatically in tibial cartilages as creep developed for both participants. At 10hrs, the maximum fluid pressures decreased to 0.05 and 0.15 MPa in the lateral compartments, and 0.13 and 0.30 MPa in the medial compartments, for Participants A and B, respectively (Fig. 8). The fluid pressures showed a similar trend to the contact pressures, which were higher in lateral than medial compartment before creep for both participants (Fig. 9). The locations of higher fluid pressure shifted from lateral to medial compartment with creep for Participant A, however it did not shift for Participant B (Fig. 9). Moreover, the locations of all maximum fluid pressures shifted to central load regions and to the deep zone of tibial cartilages with time for both participants (Fig. 9).

4. Discussion

The objectives of the present study were to evaluate the in-vivo creep behavior of human TF joints during a prolonged standing and to validate the FE model of these knee joints. This was accomplished by obtaining knee kinematics using BVR images for two participants during standing and constructing two poromechanical FE models with mechanical properties calibrated from the in-vivo data (Fig. 2). Load bearing in cartilages and menisci was explored with a model simulation of a full-range creep response of the joint. The main findings in the present study are: the subject-specific knee models were capable of mimicking the in-vivo experiments; the strain, contact and fluid pressures in the two models for different participants were notably different although the same boundary conditions and force were applied; and a typical creep behavior at the joint level was observed in both participants.

This study demonstrated a successful direct validation approach for the subject-specific poromechanical FE model of human knee joints. For both participants, the experimental vertical displacements obtained using the BVR imaging system showed good agreement with that from FE simulations of the same participants (Fig. 3). Pearson correlation coefficient was 0.99 for the validation of both models. Both participants gradually applied more than their half bodyweight on their right legs in 8–12s without any external control over the loading rate. An approximate ramp and creep load was confirmed with the measured ground

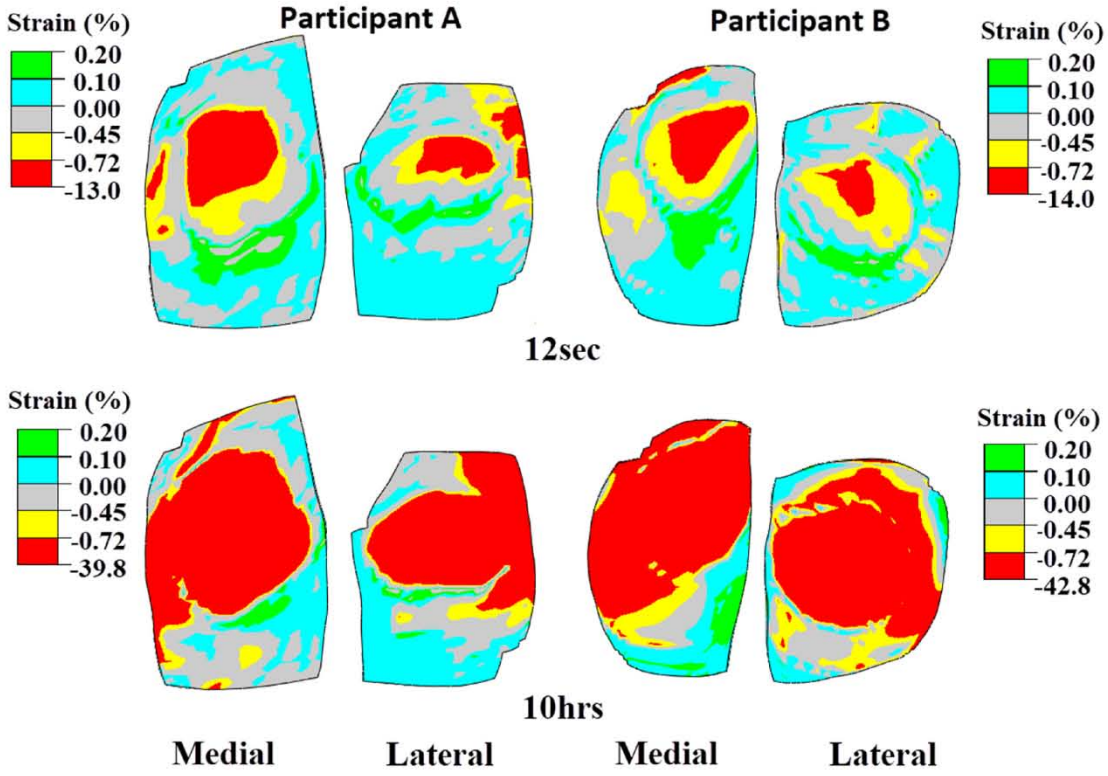

Fig. 5. Normal strain distributions in the surfaces of tibial cartilages in the direction of compression at 12s and 10hrs for both participants. (Superior view; negative value = compressive strain).

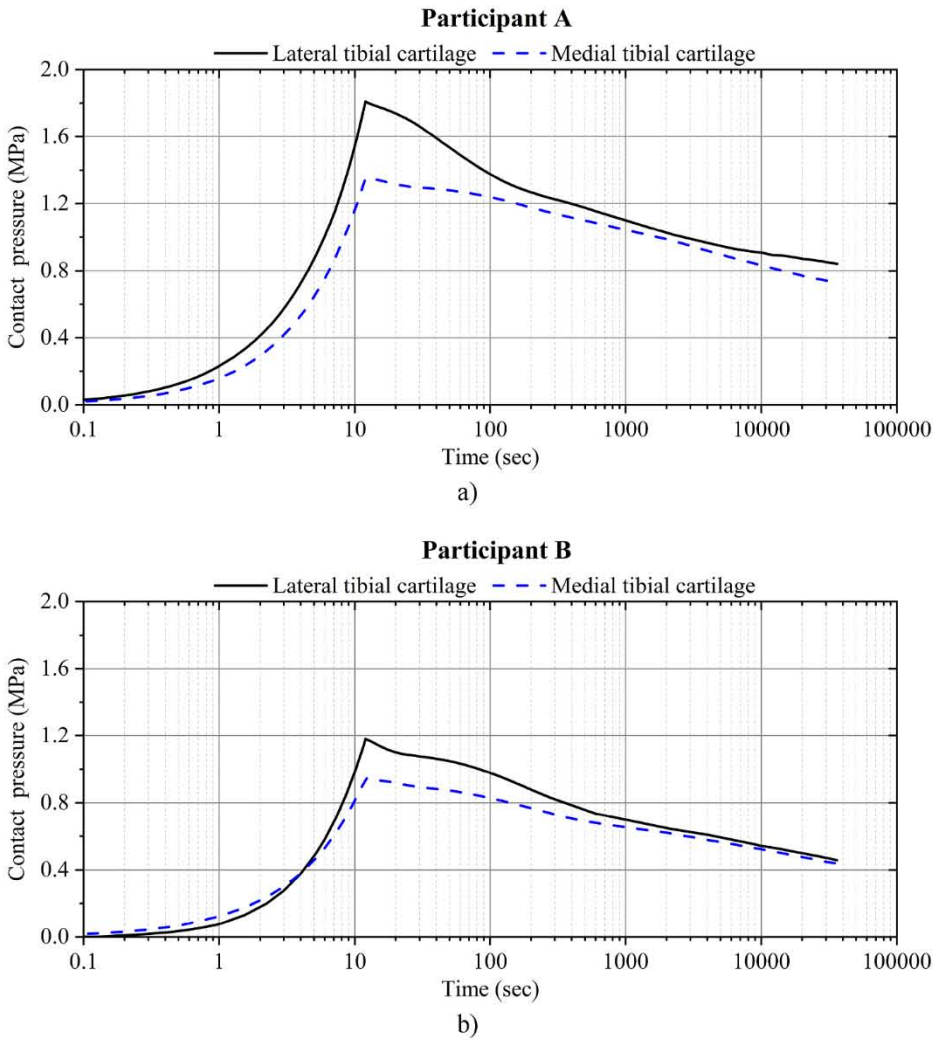

Fig. 6. Maximum contact pressures on the surfaces of tibial cartilages with standard creep loading for: **a)** Participant A; and **b)** Participant B. The locations of maximum contact pressure may change as creep develops. A logarithmic scale for time was preferred for detailed view of variation during ramp compression when the force increased from 0 to the maximum (0–12 s).

Table 2
The relationship between contact areas and average contact pressures.

	Model	Compartment	Contact area (mm^2)	Average contact pressure (MPa)
12 s.	**Participant A**	Lateral	272	0.66
		Medial	342	0.53
	Participant B	Lateral	589	0.35
		Medial	468	0.40
10 h.	**Participant A**	Lateral	440	0.41
		Medial	534	0.39
	Participant B	Lateral	800	0.25
		Medial	644	0.29

reaction forces (Fig. 3). In contrast to the in-vivo cartilage deformation available from the literature, where a full bodyweight was quickly applied (Hosseini et al., 2010), a slow ramp load was used in the present study to facilitate numerical convergence in modeling. The validation procedure is critical in obtaining sensitive and physiologically representative results with the FE studies performed on complex biological systems such as the knee joint (Cooper et al., 2019). To date, only few discrete in-vivo creep data have been used for FE knee model validation (Halonen et al., 2014). Our approach may inspire further investigations in the in-vivo contact mechanics of the knee joint for which the time-dependent behavior is essential for its mechanical function.

Substantial differences in the results were observed between the knee models of two participants, when subjected to the same compression load (390N) and boundary conditions. These differences may partially be attributed to differences in knee geometry, reported as the predominant factor influencing contact pressure distribution (Donahue et al., 2003, 2004). Six geometric parameters assumed to influence contact pressure were obtained for both joints (Fig. 10 and Table 3). These geometric parameters have been used previously in the literature (Donahue et al., 2004) to compare male and female models. For example, the sizes of the medial meniscus were evaluated owing to fact that medial meniscal parameters play an important role on the mechanics of knee joint (Majewski et al., 2006; Feeley and Lau, 2018; Uzuner et al., 2020). In the present study, the bones and cartilaginous tissues were consistently larger for Participant B (male) than Participant A (female) (difference 12–29%). This finding is consistent with the literature data (male knees are 17 ± 7% larger than female) derived from MRI scans of 118 subjects (Elsner et al., 2010). Whereas maximum and average contact pressures are more sensitive to MML and MMW, contact area and distributions of contact pressure are more sensitive to MMHC and MMLC (Donahue et al., 2004). These findings from previous studies indicate that the increase in the geometric parameters results in an increase in contact areas but a decrease in contact pressures (Donahue et al., 2004). While the current study findings are based on one

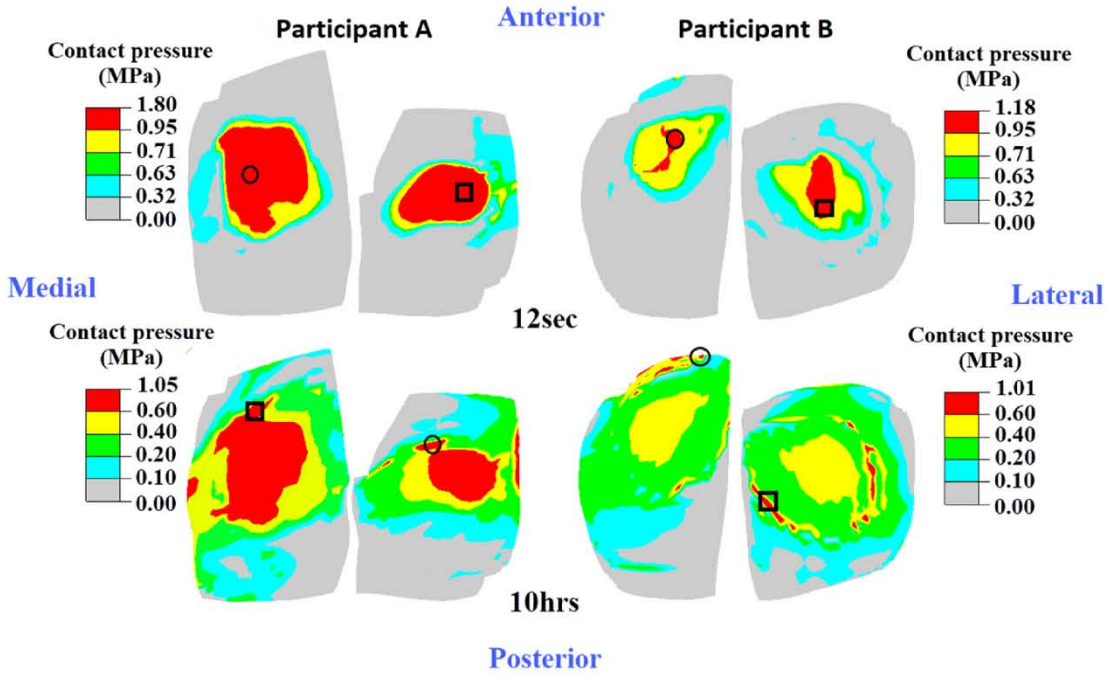

Fig. 7. Contact pressure distributions on the surfaces of medial and lateral tibial cartilages at 12sec (when creep just began) and 10hrs (when creep essentially completed) for both participants. Black circles and squares indicate the locations of maximum contact pressures for each compartment, and the squares indicate the location of the peak contact pressures across the compartments. (Superior view.)

female and one male participant, they support the previous study findings. Both MML and MMW in the male knee were approximately 14% larger than that in female (Table 3). The maximum and average contact and fluid pressures (at 12s) in the male knee were, respectively, 34%, 42%, and 29% less than that in the female (Figs. 6–9, and Table 2). Similarly, MMHC and MMLC in the male knee were approximately 29% larger than that in the female knee. The total contact area (at 12s) in medial side of the male knee was 37% larger than that of the female knee. Contact forces distributed over a larger area would result in a reduction of the contact and fluid pressures in articular cartilage (Tables 2 and 3) (Radin et al., 1984).

Other subject-specific responses include different displacements under the same compressive force. Interestingly, the vertical displacement and the strain at 10hrs of loading in the model of Participant B were, respectively, 21% and 8% larger than those of the model of Participant A (Figs. 4 and 5). Moreover, the locations of maximum fluid pressure at 12s occurred at approximately ½ depth from the tibial cartilage surfaces for Participant A, as compared to ¾ depth for Participant B (Fig. 8). These differences may be attributed to different tissue properties in the two participants (Table 1), as the stiffness of knee joint may vary individually (Granata et al., 2002). Differences were also observed in the locations of the maximum contact and fluid pressures. While the locations remained in the lateral side throughout creep for the knee of Participant B, they shifted from the lateral to medial side for Participant A (Figs. 7 and 9).

The predicted creep time in this study was greater than that reported in several studies with tissue specimens, when subjected to similar average contact pressures. The time to approach equilibrium state was roughly 7–10hrs depending on desired accuracy (Fig. 4). In contrast, the creep time of tissue discs harvested from ovine and bovine joints was 1–8 h depending on the average contact pressures (Stolberg-Stolberg et al., 2018). This difference may be explained by the simple compressive load support in an isolated tissue sample in comparison to a complex load support in an intact joint. The contact remained unchanged in most in-vitro studies performed with confined or unconfined compression tests of tissue explants (Boettcher et al., 2014; Stolberg-Stolberg et al., 2018). However, the predicted contact area for the joint increased substantially with creep in this study (Table 2).

The full-range creep response was simulated in the present study to demonstrate the influence of fluid pressurization on the load bearing in the joint and load-sharing among the cartilaginous tissues, which may play an important role in tissue integrity and health. During knee joint creep, the soft tissues experience a complex load transfer at different scales that occurs simultaneously between the fluid and tissue matrix, between tissues, between joint compartments, as well as between locations in the same compartment. A full-range creep response demonstrates the rate and magnitude of these complex load-bearing changes with time. Currently, only limited in-vivo creep data are available. The equilibrium of knee tissues in vivo has been reported to be mostly completed or approach its asymptote in 5min under 750N (Hosseini et al., 2010), 13min under 348N (Räsänen et al., 2016), and 1 h under 386N (Halonen et al., 2014) of rapidly applied forces. Our present and previous model studies revealed that the joint creep may take hours to complete under ramp loading (Fig. 4; Kazemi et al., 2011; Uzuner et al., 2019). This discrepancy could be caused by loading conditions, posture (on treadmill or MRI table), and individual differences. Although it cannot be confirmed from existing data, another potential contributor could be different loading rates, which were 32.5N/s (390N/12s) in the present study, but 120N/s (Schoenbauer et al., 2015), 348N/s (Räsänen et al., 2016) and 386N/s (Halonen et al., 2014), respectively, in other studies. That is because fluid pressurization induced creep or relaxation in cartilaginous tissues can be greatly affected by the compression rate (Li et al., 2003; Rodriguez and Li, 2017). On the other hand, the maximum axial strain in the tibial cartilage surface was approximately 40% (Fig. 5) at the equilibrium state for both participants in our study, while it was approximately 15% in other in-vivo studies (Hosseini et al., 2010; Halonen et al., 2014; Räsänen et al., 2016).

The joint displacement at the equilibrium state obtained in this study was similar to that of porcine knee joints loaded with 500N compression force of 3.24 ± 0.70 mm (Rodriguez and Li, 2017). Animal joints are widely used in mechanical tests of tissue behavior because of their wide availability, low cost, and reduced ethical concerns. However, human knee joint mechanics may be better understood with in-vivo human measurements. For example, the creep time of an intact porcine knee

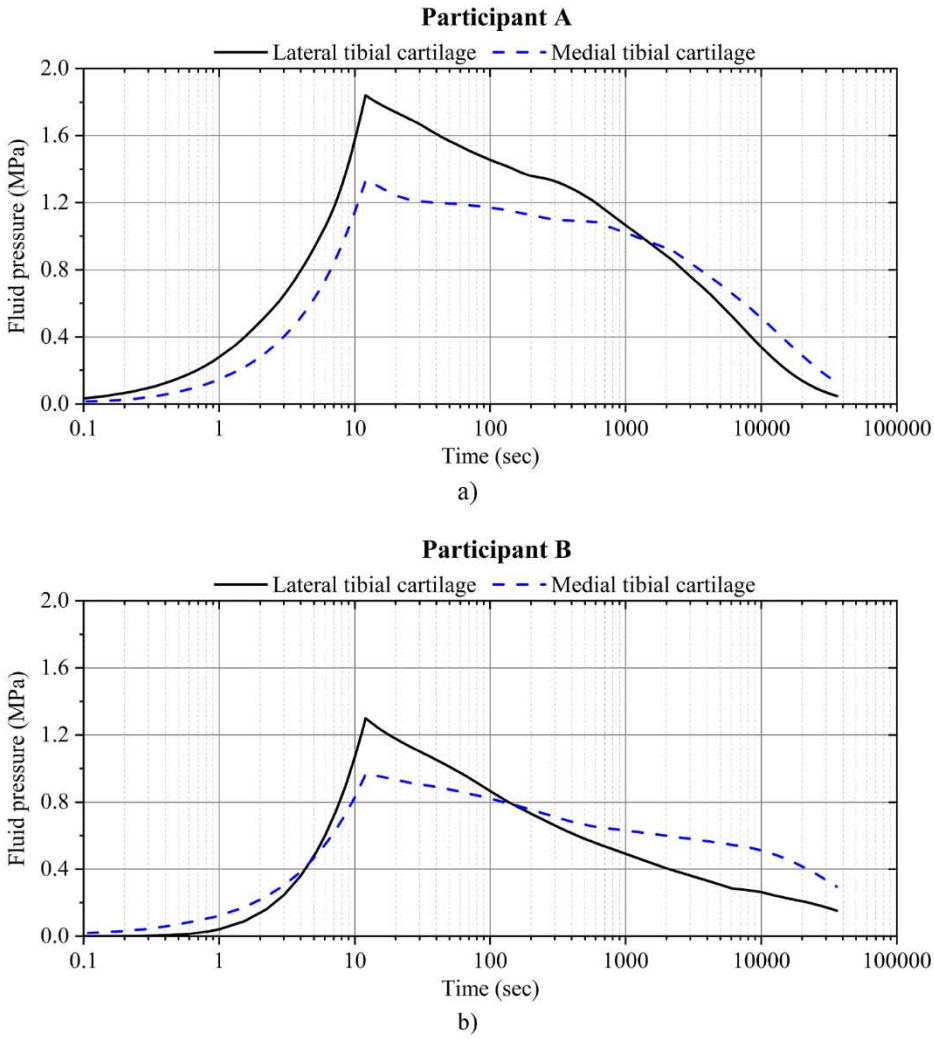

Fig. 8. Maximum fluid pressure in the tibial cartilages as a function of time for: a) Participant A; and b) Participant B. The maximum fluid pressure was obtained from the centroids of elements which were approximately at 1/2 depth from the lateral tibial surfaces for Participant A, while it was obtained approximately at 3/4 from the lateral tibial surface for Participant B.

under 500N force was not much longer than 1 h (test was only done for 1 h when creep was not fully completed), as compared to approximately 10hrs for the human knee under 390N force (Fig. 4). It is worth noting that approximately 80% of the displacement was developed in 4 h, and the increase in displacement may be neglected after 7 h.

Although different joint contacts were investigated, it may be interesting to compare our modeling results for the tibiofemoral joints with the data obtained from MRI of cadaveric femoropatellar joints (Herberhold et al., 1999), the only experimental study that shows long-term creep of knee joints. In that study, the mean compressive strain (n=6) under 150% bodyweight was estimated to be 30% for femoral cartilage after 3.5 h of creep. Of the total 30% strain developed in 3.5 h, 4% and 30% were developed, respectively, during the first minute and 8 min of creep. Our modeling results predicted a total displacement of 2.8 mm at 10 h for Participant A, of which 21% and 35% were developed, respectively, during the first minute and 10 min of creep (Fig. 4; similar results for Participant B). These modeling results compare reasonably well with that of experiments, recognizing substantial differences between the geometry and congruency of the two types of joints, and that the creep modeled in the present study was much faster in the first minute as compared to that in the experiments (21% vs 4%) of Herberhold and colleagues. Nevertheless, the contrast in the first minute was likely produced by different tissue properties, distinct contact geometries and loading conditions in different types of joints. In the first minute of the cadaveric measurements (Herberhold et al., 1999), the creep was slower in the femoral cartilage (4% in femoral vs 7% in patellar cartilages with respect to the strain at 3.5 h). Within the first 8 min, however, the creep was overall faster in the femoral cartilage (30% in femoral vs 25% in patellar cartilages with respect to the strain at 3.5 h). The creep rates were not the same in the two tissues of the same joint contact. Therefore, we do not expect the exact same creep rates in different joint contacts.

Our modeling results showed a slow fluid pressure reduction when the compressive force of the joint remained constant (Figs. 8 and 9), which implied a slow fluid exudation in the cartilaginous tissues or a slow fluid redistribution from loaded regions to unloaded regions. Our daily activities involve frequent loading and unloading cycles. When the tissues are externally loaded, only a small amount of the synovial fluid is lost from the loaded regions; when unloaded, fluid exudation is stopped or reversed. Therefore, it is unlikely healthy tissues would experience a substantial fluid loss during normal activities. For example, only 2–5% cartilage thickness changes were observed after 8-h activities (Coleman et al., 2013). – In that study, MRI of knees was obtained at 8:00am and 4:00pm when the knees were not externally loaded. Therefore, the tissue thickness changes should have been primarily caused by fluid loss in the tissues – On the other hand, our modeling results showed over 10% compressive strains in seconds (Fig. 5), as compared to the 2–5% thickness changes in 8 h, which indicates frequent fluid loss and

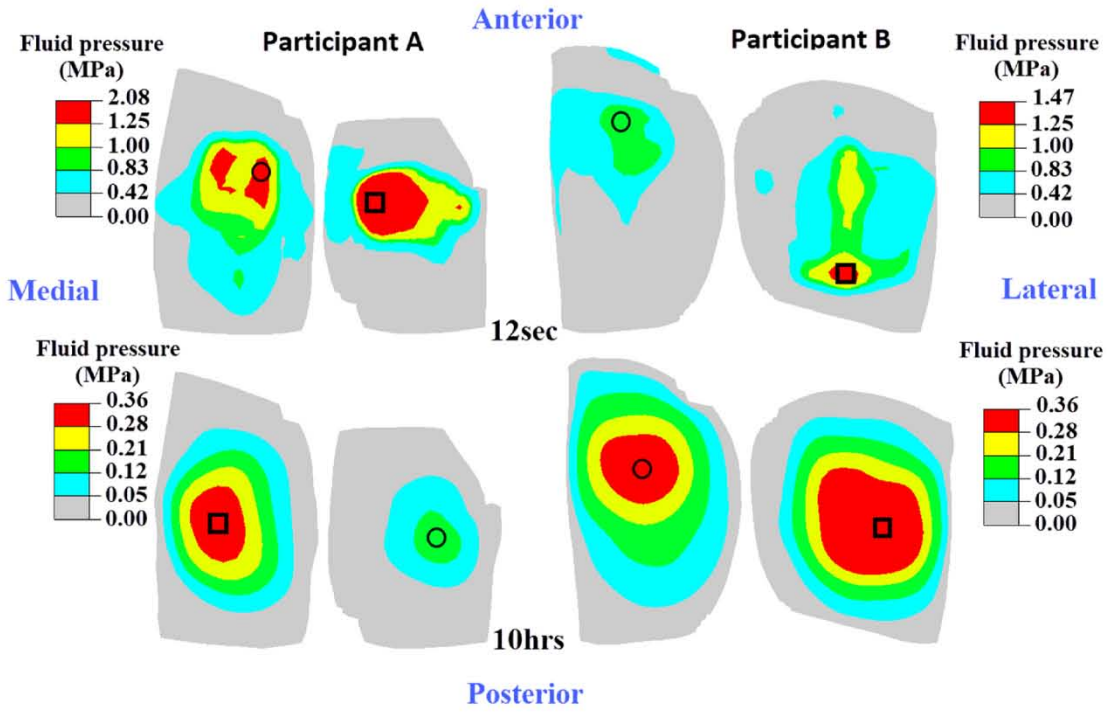

Fig. 9. Fluid pressure distributions in the tibial cartilages at 12sec (1/2 depth layer) and 10hrs (deepest layer) for both participants. Black circles and squares indicate the locations of maximum values for each compartment, and the squares indicate the location of the highest fluid pressures across the compartments. (Inferior view.)

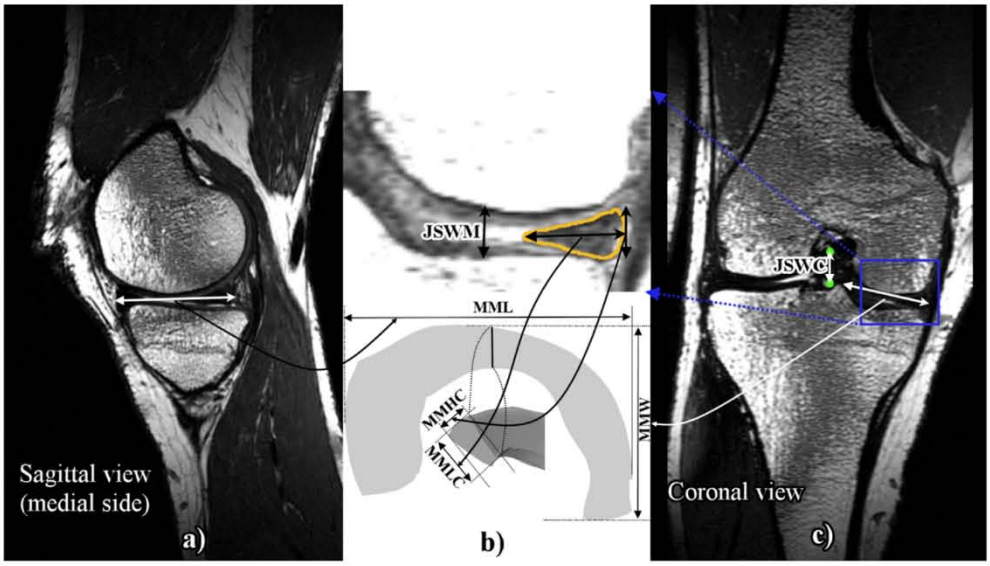

Fig. 10. Schematic of the six geometric parameters of right knee joint of Participant B. **a)** Sagittal view of medial side of the joint; **b)** Highlighted view of medial meniscus; and **c)** Coronal view of the joint. All scaling was based on the center of the weight-bearing surface. Abbreviations are as follows: JSWM, joint space width-medial side; JSWC, joint space width-center (i.e., the vertical distance between the midpoint of femoral condyle and the center of tibial spines); MML, medial meniscus length; MMW, medial meniscus width; MMHC, medial meniscus height-center edge; MMLC, medial meniscus length-center edge.

Table 3
Joint geometry of A and B participants obtained from MRI of unloaded right knees using the measurement tool within the AMIRA software. Abbreviations are defined and shown in Fig. 10.

	Participant A	Participant B
MML	39.8 mm	45.2 mm
MMW	27.5 mm	32.0 mm
MMHC	4.4 mm	6.2 mm
MMLC	7.3 mm	10.2 mm
JSWM	6.3 mm	7.7 mm
JSWC	16.3 mm	20.2 mm

recovery during daily activities.

Measurements were only performed for 10 min due to concerns over radiation and difficulties with unconstrained human participants. The displacement of the joint developed in 10 min was likely about 1/3 of the total displacement at the equilibrium of the joint (Fig. 4). Nevertheless, the 10-min measurement captured the early creep with the greatest deformation rates (Fig. 3), which reflected the elastic properties and permeabilities of the tissues, as well as early collagen viscoelasticity. However, the material properties extracted from these experimental data may only approximate other than accurately represent the long-term creep response of the knee. Other limitations of the present study include the use of vertical ground reaction forces as model input, which may not be equivalent to vertical knee joint forces. In addition, joint

contact mechanics was considered with regards to joint translations in the proximal-distal direction only. Previous FE studies showed that constraining the rotational movement of the knee joint had a significant impact on the results (Donahue et al., 2002). Further, in-vivo kinematics of the femur and tibia were obtained using BVR imaging. Resultant estimates of joint translations are influenced by the spatial resolution of the BVR system and the accuracy of the 2D-3D image registration process. As the BVR system used in this study has been validated to detect differences of 0.08 mm using bone models (Sharma et al., 2015), the resolution appears sufficient for the experimental displacements observed in this study. Adequate resolution of the BVR data was also supported by comparing geometries measured from MRI and BVR images: the vertical distance between the midpoint of femoral condyle and the center of tibial spines (JSWC) measured from the MRI was 16.3 and 20.2 mm, respectively, for Participants A and B (Table 3), as compared to 16.4 and 20.1 mm determined from the BVR images. Finally, the results obtained from the two participants only reflect the differences between the two individuals. Further studies are required to demonstrate the general mechanical behavior of a cohort or the sex difference in poromechanics of the knees.

5. Conclusion

High-speed video-radiography measurements and MRI-based finite element modeling have been performed in the present study to determine the creep response of human knee joints subjected to partial bodyweight. The data obtained from the images of both participants demonstrated substantial creep of the joint produced by cartilages and menisci during 10-min standing. This finding highlights the need to further understand the creep of knee tissues in vivo, an aspect that has been commonly neglected in the literature. This study also demonstrated the feasibility of quantifying in-vivo creep behavior of human knee joints with minimal constraints on the legs. Further, this study has demonstrated the capacity of the finite element model to capture subject-specific creep response of soft tissue structures of the knee. These combined approaches enhanced the fidelity of model results and expanded the research findings beyond in-vivo experimentation. The study design may be used for non-invasive cartilage evaluation in vivo, where the tissue properties can be extracted by finite element modeling with the creep data of the knee obtained from a prolonged standing.

CRediT authorship contribution statement

S. Uzuner: processed all BVR data, constructed MRI-based FE models, obtained all results presented and wrote the draft manuscript. **G. Kuntze:** designed MRI and BVR protocols, led the BVR measurement, supported BVR image processing and revised the manuscript. **L.P. Li:** initiated and advised the study, conceptualized and revised the manuscript. **J.L. Ronsky:** participated in the study design and BVR measurement, provided BVR lab support and revised the manuscript. **S. Kucuk:** developed a new MATLAB algorithm to improve image contrast for detection of bony edges.

Ethical approval

REB15-1165, University of Calgary, for the use of MRI and BVR of human subjects. All participant data were processed on the Calgary campuses.

Declaration of competing interest

The authors declare that they have no known competing financial interests or personal relationships that could have appeared to influence the work reported in this paper.

Acknowledgements

Sabri Uzuner received financial support from the Scientific and Technological Research Council of Turkey for doing this research at the University of Calgary. Cette recherche a été financée par le Conseil de recherches en sciences naturelles et en génie du Canada (CRSNG/NSERC). We would also like to thank Seaman Family MR Research Center for conducting the MRI of the knees and thank the research participants for their support of this study.

References

Allard, P., Blanchi, J., Aissaoui, R., 1995. Bases of three-dimensional reconstruction in three-dimensional analysis of human movement. In: Allard, P., Stokes, I., Blanchi, J. (Eds.), Human Kinetics Champaign Il, pp. 19–40.

Barron, M.C., Rubin, B.R., 2007. Managing osteoarthritic knee pain. J. Am. Osteopath. Assoc. 107 (Suppl. 6), ES21–ES27. PMCID: 17986674.

Bei, Y., Fregly, B.J., Sawyer, W.G., Banks, S.A., Kim, N.H., 2004. The relationship between contact pressure, insert thickness, and mild wear in total knee replacements. Comput. Model. Eng. Sci. 6 (2), 145–152.

Below, S., Arnoczky, S.P., Dodds, J., Kooima, C., Walter, N., 2002. The split-line pattern of the distal femur: a consideration in the orientation of autologous cartilage grafts. Arthrosc. J. Arthrosc. Relat. Surg. 18 (6), 613–617. https://doi.org/10.1053/jars.2002.29877.

Boettcher, K., Grumbein, S., Winkler, U., Nachtsheim, J., Lieleg, O., 2014. Adapting a commercial shear rheometer for applications in cartilage research. Rev. Sci. Instrum. 85 (9), 093903 https://doi.org/10.1063/1.4894820.

Boettcher, K., Kienle, S., Nachtsheim, J., Burgkart, R., Hugel, T., Lieleg, O., 2016. The structure and mechanical properties of articular cartilage are highly resilient towards transient dehydration. Acta Biomater. 29, 180–187. https://doi.org/10.1016/j.actbio.2015.09.034.

Buck, R., Wyman, B., Le Graverand, M.-P.H., Hudelmaier, M., Wirth, W., Eckstein, F., 2010. Osteoarthritis may not be a one-way-road of cartilage loss–comparison of spatial patterns of cartilage change between osteoarthritic and healthy knees. Osteoarthritis Cartilage 18 (3), 329–335. https://doi.org/10.1016/j.joca.2009.11.009.

Cao, L., Youn, I., Guilak, F., Setton, L.A., 2006. Compressive properties of mouse articular cartilage determined in a novel micro-indentation test method and biphasic finite element model. J. Biomech. Eng. 128 (5), 766–771. https://doi.org/10.1115/1.2246237.

Chan, D.D., Cai, L., Butz, K.D., Trippel, S.B., Nauman, E.A., Neu, C.P., 2016. In vivo articular cartilage deformation: noninvasive quantification of intratissue strain during joint contact in the human knee. Sci. Rep. 6 (1), 19220 https://doi.org/10.1038/srep19220.

Chen, L., Armstrong, C., Raftopoulos, D., 1994. An investigation on the accuracy of three-dimensional Space reconstruction using the direct linear transformation technique. J. Biomech. 27 (4), 493–500. https://doi.org/10.1016/0021-9290(94)90024-8.

Choi, J.-H., McWalter, E., Datta, S., Mueller, K., Maier, A., Fahrig, R., Levenston, M., Gold, G., 2016. Tibial cartilage creep during weight bearing: in vivo 3D CT assessment. Osteoarthritis Cartilage 24, S104. https://doi.org/10.1016/j.joca.2016.01.210.

Coleman, J.L., Widmyer, M.R., Leddy, H.A., Utturkar, G.M., Spritzer, C.E., Moorman III, C.T., Guilak, F., DeFrate, L.E., 2013. Diurnal variations in articular cartilage thickness and strain in the human knee. J. Biomech. 46, 541–547. https://doi.org/10.1016/j.jbiomech.2012.09.013.

Cooper, R.J., Wilcox, R.K., Jones, A.C., 2019. Finite element models of the tibiofemoral joint: a review of validation approaches and modelling challenges. Med. Eng. Phys. https://doi.org/10.1016/j.medengphy.2019.08.002.

Dabiri, Y., Li, L.P., 2013. Altered knee joint mechanics in simple compression associated with early cartilage degeneration. Comput Math Methods Med 2013 (Special Issue), 11. https://doi.org/10.1155/2013/862903.

Dassault Systems, Abaqus, V., 2016. 6.14, Online Documentation Help, Theory Manual. Velizy-Villacoublay, France.

Donahue, T.L.H., Hull, M.L., Rashid, M.M., Jacobs, C.R., 2002. A finite element model of the human knee joint for the study of tibio-femoral contact. J. Biomech. Eng. 124 (3), 273–280. https://doi.org/10.1115/1.1470171.

Donahue, T.L.H., Hull, M.L., Rashid, M.M., Jacobs, C.R., 2003. How the stiffness of meniscal attachments and meniscal material properties affect tibio-femoral contact pressure computed using a validated finite element model of the human knee joint. J. Biomech. 36 (1), 19–34. https://doi.org/10.1016/S0021-9290(02)00305-6.

Donahue, T.L.H., Hull, M.L., Rashid, M.M., Jacobs, C.R., 2004. The sensitivity of tibiofemoral contact pressure to the size and shape of the lateral and medial menisci. J. Orthop. Res. 22 (4), 807–814. https://doi.org/10.1016/j.orthres.2003.12.010.

Eckstein, F., Wirth, W., 2011. Quantitative cartilage imaging in knee osteoarthritis, 2011 Arthritis 19, 475684. https://doi.org/10.1155/2011/475684.

Eckstein, F., Maschek, S., Wirth, W., Hudelmaier, M., Hitzl, W., Wyman, B., Nevitt, M., Le Graverand, M.H., Group, O.I., 2009. One year change of knee cartilage morphology in the first release of participants from the Osteoarthritis Initiative progression subcohort: association with sex, body mass index, symptoms and radiographic osteoarthritis status. Ann. Rheum. Dis. 68 (5), 674–679. https://doi.org/10.1136/ard.2008.089904.

Elsner, J.J., Portnoy, S., Guilak, F., Shterling, A., Linder-Ganz, E. J. J. o. b. e., 2010. MRI-based characterization of bone anatomy in the human knee for size matching of a medial meniscal implant, 132. https://doi.org/10.1115/1.4002490, 10.

Erdemir, A., Besier, T.F., Halloran, J.P., Imhauser, C.W., Laz, P.J., Morrison, T.M., Shelburne, K.B., 2019. Deciphering the "Art" in modeling and simulation of the knee joint: overall strategy. J. Biomech. Eng. 141 (7) https://doi.org/10.1115/1.4043346.

Feeley, B.T., Lau, B.C., 2018. Biomechanics and clinical outcomes of partial meniscectomy. JAAOS-Journal of the American Academy of Orthopaedic Surgeons 26 (24), 853–863. https://doi.org/10.5435/JAAOS-D-17-00256.

Felson, D.T., 2006. Osteoarthritis of the knee. N. Engl. J. Med. 354 (8), 841–848. https://doi.org/10.1056/NEJMcp051726.

Felson, D.T., Naimark, A., Anderson, J., Kazis, L., Castelli, W., Meenan, R.F., 1987. The prevalence of knee osteoarthritis in the elderly. The Framingham Osteoarthritis Study. Arthritis Rheum.: Official Journal of the American College of Rheumatology 30 (8), 914–918. https://doi.org/10.1002/art.1780300811.

Granata, K.P., Wilson, S.E., Padua, D.A., 2002. Gender differences in active musculoskeletal stiffness. Part I.: quantification in controlled measurements of knee joint dynamics. J. Electromyogr. Kinesiol. 12 (2), 119–126. https://doi.org/10.1016/S1050-6411(02)00002-0.

Grood, E.S., Suntay, W.J., 1983. A joint coordinate system for the clinical description of three-dimensional motions: application to the knee. J. Biomech. Eng. 105 (2), 136–144. https://doi.org/10.1115/1.3138397.

Gu, K.B., Li, L.P., 2011. A human knee joint model considering fluid pressure and fiber orientation in cartilages and menisci. Med. Eng. Phys. 33 (4), 497–503. https://doi.org/10.1016/j.medengphy.2010.12.001.

Halonen, K., Mononen, M., Jurvelin, J., Töyräs, J., Salo, J., Korhonen, R., 2014. Deformation of articular cartilage during static loading of a knee joint–experimental and finite element analysis. J. Biomech. 47 (10), 2467–2474. https://doi.org/10.1016/j.jbiomech.2014.04.013.

Herberhold, C., Stammberger, T., Faber, S., Putz, R., Englmeier, K.H., Reiser, M., Eckstein, F., 1998. An MR-based technique for quantifying the deformation of articular cartilage during mechanical loading in an intact cadaver joint. Magn. Reson. Med. 39 (5), 843–850. https://doi.org/10.1002/mrm.1910390522.

Herberhold, C., Faber, S., Stammberger, T., Steinlechner, M., Putz, R., Englmeier, K., Reiser, M., Eckstein, F., 1999. In situ measurement of articular cartilage deformation in intact femoropatellar joints under static loading. J. Biomech. 32 (12), 1287–1295. https://doi.org/10.1016/S0021-9290(99)00130-X.

Hosseini, A., Van de Velde, S.K., Kozanek, M., Gill, T.J., Grodzinsky, A.J., Rubash, H.E., Li, G., 2010. In-vivo time-dependent articular cartilage contact behavior of the tibiofemoral joint. Osteoarthritis Cartilage 18 (7), 909–916. https://doi.org/10.1016/j.joca.2010.04.011.

Kazemi, M., Li, L.P., 2014. A viscoelastic poromechanical model of the knee joint in large compression. Med. Eng. Phys. 36 (8), 998–1006. https://doi.org/10.1016/j.medengphy.2014.04.004.

Kazemi, M., Li, L.P., Savard, P., Buschmann, M.D., 2011. Creep behavior of the intact and meniscectomy knee joints. Journal of the Mechanical Behavior of Biomedical Materials 4 (7), 1351–1358. https://doi.org/10.1016/j.jmbbm.2011.05.004.

Kiapour, A., Kiapour, A.M., Kaul, V., Quatman, C.E., Wordeman, S.C., Hewett, T.E., Demetropoulos, C.K., Goel, V.K., 2014. Finite element model of the knee for investigation of injury mechanisms: development and validation. J. Biomech. Eng. 136 (1) https://doi.org/10.1115/1.4025692.

Li, L.P., Buschmann, M.D., Shirazi-Adl, A., 2002. The role of fibril reinforcement in the mechanical behavior of cartilage. Biorheology 39 (1, 2), 89–96.

Li, L.P., Buschmann, M.D., Shirazi-Adl, A., 2003. Strain-rate dependent stiffness of articular cartilage in unconfined compression. J. Biomech. Eng. 125 (2), 161–168. https://doi.org/10.1115/1.1560142.

Li, L.P., Herzog, W., 2004. The role of viscoelasticity of collagen fibers in articular cartilage: theory and numerical formulation. Biorheology 41, 181–194.

Li, J.-S., Tsai, T.-Y., Wang, S., Li, P., Kwon, Y.-M., Freiberg, A., Rubash, H.E., Li, G., 2014. Prediction of in vivo knee joint kinematics using a combined dual fluoroscopy imaging and statistical shape modeling technique. J. Biomech. Eng. 136 (12), 124503 https://doi.org/10.1115/1.4028819.

Lichti, D.D., Sharma, G.B., Kuntze, G., Mund, B., Beveridge, J.E., Ronsky, J.L., 2015. Rigorous geometric self-calibrating bundle adjustment for a dual fluoroscopic imaging system. IEEE Trans. Med. Imag. 34 (2), 589–598. https://doi.org/10.1109/TMI.2014.2362993.

Liu, F., Kozanek, M., Hosseini, A., Van de Velde, S.K., Gill, T.J., Rubash, H.E., Li, G., 2010. In vivo tibiofemoral cartilage deformation during the stance phase of gait. J. Biomech. 43 (4), 658–665. https://doi.org/10.1016/j.jbiomech.2009.10.028.

Lohmander, L.S., Englund, P.M., Dahl, L.L., Roos, E.M., 2007. The long-term consequence of anterior cruciate ligament and meniscus injuries: osteoarthritis. Am. J. Sports Med. 35 (10), 1756–1769. https://doi.org/10.1177/0363546507307396.

Majewski, M., Susanne, H., Klaus, S., 2006. Epidemiology of athletic knee injuries: a 10-year study. Knee 13 (3), 184–188. https://doi.org/10.1016/j.knee.2006.01.005.

Maniwa, S., Nishikori, T., Furukawa, S., Kajitani, K., Ochi, M., 2001. Alteration of collagen network and negative charge of articular cartilage surface in the early stage of experimental osteoarthritis. Arch. Orthop. Trauma Surg. 121 (4), 181–185.

Peña, E., Calvo, B., Martinez, M.A., Doblaré, M., 2006. A three-dimensional finite element analysis of the combined behavior of ligaments and menisci in the healthy human knee joint. J. Biomech. 39 (9), 1686–1701. https://doi.org/10.1016/j.jbiomech.2005.04.030.

Radin, E.L., de Lamotte, F., Maquet, P., 1984. Role of the menisci in the distribution of stress in the knee. Clin. Orthop. Relat. Res. (185), 290–294. PMCID: 6546709.

Räsänen, L.P., Tanska, P., Mononen, M.E., Lammentausta, E., Zbýň, Š., Venäläinen, M.S., Szomolanyi, P., van Donkelaar, C.C., Jurvelin, J.S., Trattnig, S., 2016. Spatial variation of fixed charge density in knee joint cartilage from sodium MRI–Implication on knee joint mechanics under static loading. J. Biomech. 49 (14), 3387–3396. https://doi.org/10.1016/j.jbiomech.2016.09.011.

Rodriguez, M.L., Li, L., 2017. Compression-rate-dependent nonlinear mechanics of normal and impaired porcine knee joints. BMC Muscoskel. Disord. 18 (1), 447. https://doi.org/10.1186/s12891-017-1805-9.

Roos, E.M., Roos, H., Ekdahl, C., Lohmander, L., 1998. Knee injury and osteoarthritis outcome score (KOOS)-validation of a Swedish version. Scand. J. Med. Sci. Sports 8 (6), 439–448. https://doi.org/10.1111/j.1600-0838.1998.tb00465.x.

Salaffi, F., Carotti, M., Stancati, A., Grassi, W., 2005. Health-related quality of life in older adults with symptomatic hip and knee osteoarthritis: a comparison with matched healthy controls. Aging Clin. Exp. Res. 17 (4), 255–263. https://doi.org/10.1007/BF03324607.

Schoenbauer, E., Szomolanyi, P., Shiomi, T., Juras, V., Zbýň, Š., Zak, L., Weber, M., Trattnig, S., 2015. Cartilage evaluation with biochemical MR imaging using in vivo Knee compression at 3 T-comparison of patients after cartilage repair with healthy volunteers. J. Biomech. 48 (12), 3349–3355. https://doi.org/10.1016/j.jbiomech.2015.06.016.

Shapiro, R., 1978. Direct linear transformation method for three-dimensional cinematography. Research Quarterly 49 (2), 197–205. https://doi.org/10.1080/10671315.1978.10615524.

Sharma, G.B., Kuntze, G., Kukulski, D., Ronsky, J.L., 2015. Validating dual fluoroscopy system capabilities for determining in-vivo knee joint soft tissue deformation: a strategy for registration error management. J. Biomech. 48 (10), 2181–2185. https://doi.org/10.1016/j.jbiomech.2015.04.045.

Shiomi, T., Nishii, T., Tamura, S., Tanaka, H., Murase, K., Yoshikawa, H., Sugano, N., 2012. Influence of medial meniscectomy on stress distribution of the femoral cartilage in porcine knees: a 3D reconstructed T2 mapping study. Osteoarthritis Cartilage 20 (11), 1383–1390. https://doi.org/10.1016/j.joca.2012.07.015.

Shirazi, R., Shirazi-Adl, A., Hurtig, M., 2008. Role of cartilage collagen fibrils networks in knee joint biomechanics under compression. J. Biomech. 41 (16), 3340–3348. https://doi.org/10.1016/j.jbiomech.2008.09.033.

Shriram, D., Kumar, G.P., Cui, F., Lee, Y.H.D., Subburaj, K., 2017. Evaluating the effects of material properties of artificial meniscal implant in the human knee joint using finite element analysis. Sci. Rep. 7 (1), 1–11. https://doi.org/10.1038/s41598-017-06271-3.

Song, Y., Greve, J., Carter, D., Koo, S., Giori, N., 2006. Articular cartilage MR imaging and thickness mapping of a loaded knee joint before and after meniscectomy. Osteoarthritis Cartilage 14 (8), 728–737. https://doi.org/10.1016/j.joca.2006.01.011.

Stolberg-Stolberg, J., Foehr, P., Pflieger, I., Kuntz, L., von Deimling, C., Obermeier, A., Prodinger, P.M., Grosse, C.U., Burgkart, R., 2018. Analysis of cartilage creep recovery using a highly dynamic closed-loop test system. JBE 15 (6), 1057–1066. https://doi.org/10.1007/s42235-018-0093-x.

Tissakht, M., Ahmed, A., 1995. Tensile stress-strain characteristics of the human meniscal material. J. Biomech. 28 (4), 411–422. https://doi.org/10.1016/0021-9290(94)00081-E.

Trad, Z., Barkaoui, A., Chafra, M., 2017. A three dimensional finite element analysis of mechanical stresses in the human knee joint: problem of cartilage destruction. Journal of Biomimetics, Biomaterials and Biomedical Engineering. Trans Tech Publ, pp. 29–39. https://doi.org/10.4028/www.scientific.net/JBBBE.32.29.

Uzuner, S., Rodriguez, M.L., Li, L.P., Kucuk, S., 2019. Dual fluoroscopic evaluation of human tibiofemoral joint kinematics during a prolonged standing: a pilot study. Engineering Science and Technology, an International Journal 22 (3), 794–800. https://doi.org/10.1016/j.jestch.2018.12.014.

Uzuner, S., Li, L., Kucuk, S., Memisoglu, K., 2020. Changes in knee joint mechanics after medial meniscectomy determined with a poromechanical model. J. Biomech. Eng. 142 (10), 101006 https://doi.org/10.1115/1.4047343.

Waite, J., Beard, D., Dodd, C., Murray, D., Gill, H., 2005. In vivo kinematics of the ACL-deficient limb during running and cutting. Knee Surg. Sports Traumatol. Arthrosc. 13 (5), 377–384. https://doi.org/10.1007/s00167-004-0569-6.

Wang, H., Koff, M.F., Potter, H.G., Warren, R.F., Rodeo, S.A., Maher, S.A., 2015. An MRI-compatible loading device to assess knee joint cartilage deformation: effect of preloading and inter-test repeatability. J. Biomech. 48 (12), 2934–2940. https://doi.org/10.1016/j.jbiomech.2015.08.006.

Woo, S.L.Y., Akeson, W.H., Jemmott, G.F., 1976. Measurements of nonhomogeneous, directional mechanical properties of articular cartilage in tension. J. Biomech. 9 (12), 785–791. https://doi.org/10.1016/0021-9290(76)90186-X.

Zhang, L.-Q., Shiavi, R.G., Limbird, T.J., Minorik, J.M., 2003. Six degrees-of-freedom kinematics of ACL deficient knees during locomotion—compensatory mechanism. Gait Posture 17 (1), 34–42. https://doi.org/10.1016/S0966-6362(02)00052-8.